Phase tailoring and color-tunable luminescence of $LaNbO_4:Tb^{3+},Eu^{3+}$ nanophosphors for deep UV-pumped pc-WLEDs application

Meiting Li[a,b*], Bingxin Yuan[a], Xiangyang Zheng[a], Bo Chen[a], Chi Zhang[a], Xuejiao Wang[c], Ji-Guang Li[b*]

[a]School of Materials Science and Engineering, Liaoning University of Technology, Jinzhou, Liaoning 121001, China

[b]Research Center for Electronic and Optical Materials, National Institute for Materials Science, Tsukuba, Ibaraki 305-0047, Japan

[c]College of Chemistry and Materials Engineering, Bohai University, Jinzhou, Liaoning 121007, China

*Corresponding author

Dr. Meiting Li

Liaoning University of Technology

Tel: +86-416-4198730

E-mail: limeiting@aliyun.com

Dr. Ji-Guang Li

National Institute for Materials Science

Tel: +81-29-860-4394

E-mail: LI.Jiguang@nims.go.jp

Abstract

A series of $LaNbO_4:RE^{3+}$ (RE=Tb and Eu) phosphors were successfully synthesized via a calcination-assisted hydrothermal reaction, where the vital roles of solution pH, calcination temperature and NbO_4^{3-}/La^{3+} molar ratio in phase/morphology evolution of $LaNbO_4$ nanocrystals were elaborated. It was unambiguously demonstrated that monoclinic $LaNbO_4$ can be crystallized at solution pH=8-13 after calcination at 900 ºC. With pH=10 precursor for example, higher calcination temperature led to phase transformation from orthorhombic to monoclinic structure. $LaNbO_4$ nanoparticles exhibit self-activated broad-band excitations ($^1A_1 \rightarrow {}^1T_{1,2}$) and emissions ($^3T_{2,1} \rightarrow {}^1A_1$) within the NbO_4^{3-} ligand. Intriguingly, Tb^{3+}/Eu^{3+} incorporations allow for phase tailoring and full-visible-spectrum color-tunable luminescence, where the latter benefits from the effective $NbO_4^{3-} \rightarrow Tb^{3+} \rightarrow Eu^{3+}$ energy transfer. $LaNbO_4:0.01Tb^{3+},0.01Eu^{3+}$ phosphor exhibits stronger white-light emission, which gradually drifts to yellowish green at high heating temperature. This phosphor is an attractive candidate for optical thermometers and warm pc-WLED owning to excellent thermal stability, a low correlated color temperature of ~5694 K and a high color rendering index of ~90.

Keywords: $LaNbO_4:Tb^{3+},Eu^{3+}$ WLEDs; phase tailoring; muticolor luminescence; $NbO_4^{3-} \rightarrow Tb^{3+} \rightarrow Eu^{3+}$ energy transfer; optical thermometers

1. Introduction

White light emitting diode (WLEDs) are regarded as an indispensable solid-state light-emitting device, which has desirable merits of high luminous efficiency, energy saving, long lifetime and environmental protection, and so forth [1]. They can cover the full-visible light in the spectral range of ~400-750 nm and exhibits high color rendering index, which is recognized as a fourth-generation light source to replace traditional incandescent lamp and fluorescent lamp. Currently, WLEDs have two kinds of preparation processing, that is, multi-chip and single-chip modules [2]. In the former case, white light can be obtained by integrating single blue, green and red LED chips, however, the practical development is rather limited by the sophisticated and expensive LED circuitry [3]. The commercial single-chip WLEDs are constituted of blue GaN/InGaN chip and yellow-emitting $Y_3Al_5O_{12}:Ce^{3+}$ ($YAG:Ce^{3+}$) phosphor, nevertheless, the loss of red component results in a high correlated color temperature (CCT) and a low color rendering index (CRI), and constant cold white light will bring about asthenopia and brain damage [4]. Therefore, previous studies proposed that red/green/blue (RGB) tri-phosphors were accurately executed by introducing the sensitizer/activator combinations into host and their energy transfer (CT) under NUV LED chip excitation. Though this phosphor-converted (pc-) WLEDs exhibit lower CCT and higher CRI, the thermal quenching is detrimental to color balance between components [5]. Meanwhile, the inevitable reabsorption of phosphors lowers the luminescence efficiency of white light [6]. In this regard, the integration of high-quality pc-WLED devices are still confronted with challenges.

Up to date, considerable efforts have devoted to design advanced single-component white phosphor depositing on a UV or near-UV (NUV) LED chip, because it has the merits of better color stability, less current drooping and binning for high-power WLED application, compared with blue-triggered one [7]. The effective strategies include (1) "host + activator" combinations; (2) codoping of multi-colored activators, such as Tm^{3+}/Dy^{3+}, Tb^{3+}/Sm^{3+}, $Tm^{3+}/Tb^{3+}/Eu^{3+}$, $Yb^{3+}/Er^{3+}/Tm^{3+}$; (3) sensitizer/activator pairs and their energy transfer, including $Ce^{3+} \rightarrow Eu^{2+}$, $Ce^{3+} \rightarrow Mn^{2+}$, $Ce^{3+} \rightarrow Tb^{3+} \rightarrow Mn^{2+}$, $Eu^{2+} \rightarrow Mn^{2+}$, $Bi^{3+} \rightarrow Eu^{3+}$, *etc*.; (4) defect-related optical materials [8]. The highly-charged transition metal ions with d^0 electronic configuration, such as TiO_4^{2-}, WO_4^{2-}, WO_6^{6-}, MoO_4^{2-}, VO_4^{3-}, NbO_4^{3-}, TaO_4^{3-}, have been conceived as satisfactory fluorescence centers owning to their self-activated broadband emissions upon UV excitation and host sensitization of ligand $\rightarrow RE^{3+}$ energy transfer [9]. Wang et al., for example, hydrothermally synthesized thermodynamically stable t-$(Gd_{0.94}Eu_{0.06})(P_{0.01}V_{0.01})O_4:Eu^{3+}$ nanocrystallites, and 1 at% VO_4^{3-} separately pronounced the orange and red emissions by ~1.4 and 6 times via cooperative energy transfer of $VO_4^{3-}/Gd^{3+} \rightarrow Eu^{3+}$ [10].

$LaNbO_4$ exhibits low phonon frequency, high ionic and electronic conductivity, excellent mechanical/chemical stability and optical properties, which may find potential applications in optical storage [11], light-emitting diodes [12], 3D display solid-state lasers [13], fuel cell anodes [14,15], gas sensors [16]. A solid-state reaction is commonly employed in $LaNbO_4$ synthesis because monomeric NbO_4^{3-} is hardly dissociated in aqueous solution, but a harsh high temperature (>1000 °C) and

uncontrollable shape/size for coarse aggregates seriously restrict the functionalization applications [17]. Hydro-/solvo-thermal synthesis routes can comprehensively regulate phase structure and morphology of a compound via rational design of reaction parameters, and even govern photoluminescence performance. With citrate as a chelating agent, Li et al. produced β-$NaYF_4$:Tb^{3+} octadecahedron, microrod and hexagonal microprism, and found that octadecahedron exhibited the strongest Tb^{3+} emission [18]. It was reported that compared with bulk materials, quasi-equiaxial nanocrystals allowed more activator ions to reside onto or near the surface regions owning to their virtues of small particle size, large specific surface area and high surface activity, and thus, remarkably changed relative intensity of the electric dipole and magnetic dipole transition of RE^{3+} (RE=Eu and Dy), and also luminous colors [19].

Inspired by the fact that the inherently blue-emitting characteristics of NbO_4^{3-} ligand can fulfill emission-color tailoring combined with appropriate concentration and types of activators. We thus adopted calcination-assisted hydrothermal synthesis strategy for full color-emitting $LaNbO_4$:Tb^{3+},Eu^{3+} nanocrystals in this work, and the underlying mechanisms of crystallization kinetics, NbO_4^{3-} → Tb^{3+} → Eu^{3+} cooperative energy transfer and thermal quenching were also deciphered. The optical properties of pc-WLED fabricated by $LaNbO_4$:$0.01Tb^{3+}$,$0.01Eu^{3+}$ white-emitting phosphor in combination with 275 nm UV chip were also investigated in detail, and this warm WLED device possesses a high CRI (~90) and a low CCT (5694 K).

2. Experimental section

2.1 Reagents

The starting chemicals of $La(NO_3)_3 \cdot 6H_2O$ (>99.99% pure), $Eu(NO_3)_3 \cdot 6H_2O$ (>99.99% pure), $Tb(NO_3)_3 \cdot 5H_2O$ (>99.9% pure), Nb_2O_5 (>99.9% pure) and La_2O_3 (>99.99% pure) were purchased from Shanghai Aladdin Biochemical Technology Co., Ltd.. $NbCl_5$ (>99.0% pure) and NaOH (>97.0% pure) were purchased from Shanghai Macklin Biochemical Technology Co., Ltd.. Nitric acid (HNO_3, ultrahigh purity, analytical grade) was purchased from Jinzhou Gucheng Chemical Reagent Co., Ltd.. Milli-Q filtered water (resistivity ~18.2 MΩ cm) was used throughout the experiments. All of the reagents were used without further purification.

2.2 Preparation of $LaNbO_4:Tb^{3+},Eu^{3+}$ phosphors

In a typical procedure of calcination-assisted hydrothermal synthesis of $LaNbO_4$ micro/nanocrystals, a certain amount of $NbCl_5$ was dispersed into aqueous solution, followed by magnetic stirring for 30 min at room temperature, addition of 2 mmol of La^{3+}, and pH adjustment with dilute HNO_3 and/or NaOH solution. After continuously stirring with 30 min, 60 mL of resultant homogeneous suspension was immediately transferred into 100 mL Teflon-lined stainless steel autoclave for 24 h of reaction at 200 ºC in a preheated electric oven. After natural cooling to ambient temperature, the white precipitate was collected via centrifugation, washed with distilled water three times and absolute ethanol once to the removal of byproducts, followed by air drying at 70 ºC for 24 h. Calcination of the precursor was performed in stagnant air at a predetermined temperature for 2 h, using heating and cooling rate of 5 ºC/min at the ramp stage. The synthesis parameters including NbO_4^{3-}/La^{3+} molar ratio (R=0.75, 1, 1.2, 1.5, 2, 3 and 4),

solution pH (2-13) and calcination temperature (300-900 ºC) were systematically varied to identify reaction kinetic and phase/morphology evolution of the products. A series of $LaNbO_4$:$x$$Tb^{3+}$,$y$$Eu^{3+}$ (x=0-0.05, y=0-0.07) phosphors were prepared by the above protocol at the fixed NbO_4^{3-}/RE^{3+} molar ratio R of 1, solution pH of 10, 24 h hydrothermal reaction of 200 ºC, and subsequent calcination at 900 ºC.

The $LaNbO_4$ counterpart was prepared via a conventional solid-state reaction for comparison, and the synthesis process is briefly described as follows. 5 mmol of La_2O_3 and Nb_2O_5 were mixed and adequately grinded in an agate mortar for 6 h with the aid of appropriate ethanol. After air drying at 70 ºC for 24 h, the powder was air-calcined in a muffle furnace at 800, 900, 1000 and 1200 ºC for 6 h with heating and cooling rate of 5 ºC/min, respectively.

2.3 Encapsulation of LED devices

The as-synthesized white light-emitting $LaNbO_4$:0.01Tb^{3+},0.01Eu^{3+} phosphor was dispersed into UV curing agent (Leaftop 6300) under the mass ratio of 1:1. The mixture was stirred thoroughly and aged for 15 min to eliminate bubbles, and then uniformly casted on the surface of a commercial 275 nm LED chip (0.2 W, San'an Optoelectronics Co., Ltd.) followed by 6 h drying at 70 ºC for further measurements.

2.4 Characterization techniques

Phase identification was detected by X-ray diffractometry (XRD, Model D/max-2500 PC, Rigaku, Tokyo, Japan), using nickel filtered Cu-Kα radiation (λ=0.15406 nm, 40 kV/100 mA) and a scan rate of 6.0 º/min. Rietveld refinement of the XRD pattern was conducted using the TOPAS 4.2 software [20]. Morphology and microstructure were characterized by field emission scanning electron microscopy (FE-SEM, Model

Sigma 500, Carl Zeiss, Oberkochen, Germany) under an acceleration voltage of 10 kV and transmission electron microscopy (TEM, Model JEM-2100F, JEOL, Tokyo) under 200 kV. Thermogravimetry/differential scanning calorimeter (TG/DSC, Model STA449F3, Jupiter, NETZSCH, Germany) was measured in flowing simulated argon (80 mL min^{-1}) at a heating rate of 10 ºC min^{-1}, and the furnace temperature ranged from R.T. to 1100 ºC. The photoluminescence, absolute quantum yield and fluorescence decay curves were obtained by identical instrument with a Model FLS-1000 fluorescence spectrometer (Edinburgh Instruments, Ltd. Livingston, UK) equipped with a 450 W Xe lamp for excitation and a TAP-02 high temperature controller for the temperature-dependent luminescence and decay kinetics. Electroluminescence performances of LEDs were evaluated using an OHSP-350M LED Fast-Scan Spectrophotometer (Hangzhou Hopoo Light&Color Technology Co., Ltd, China) under a current range of 20-120 mA in the spectral range of 350-1050 nm.

3. Results and discussion

3.1 Phase structure and morphology evolution of $LaNbO_4$ nanocrystals

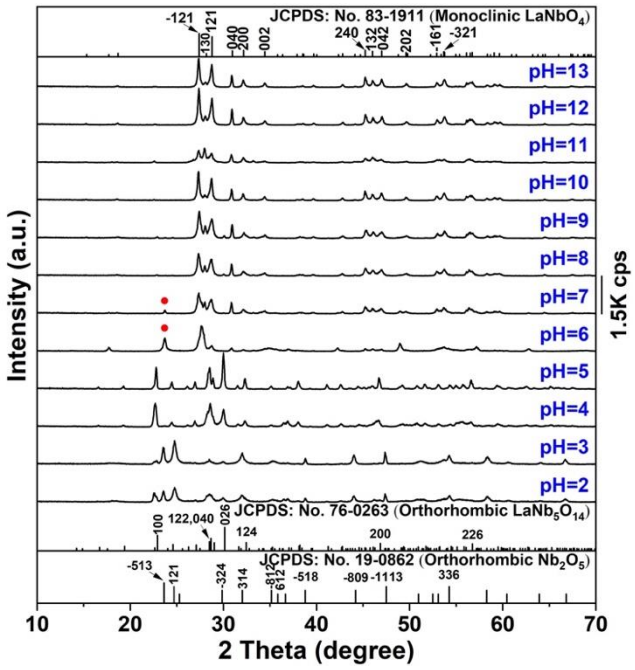

Fig. 1 XRD patterns for the products hydrothermally synthesized under various solution pH after calcination at 900 ºC. The vertical bars denote the standard diffractions of monoclinic $LaNbO_4$, orthorhombic $LaNb_5O_{14}$ and orthorhombic Nb_2O_5 for comparison.

Fig. S1 shows the powder XRD patterns of the precursors obtained via hydrothermal reaction at 200 ºC for 24 h with the solution pH values increasing from 2 to 13. It is clear that a phase mixture of hexagonal (h-) $La(OH)_3$ (JCPDS No. 01-083-2034) and orthorhombic (o-) $LaNb_5O_{14}$ (JCPDS No. 01-076-0263) was found in strong alkaline solutions (pH=~10-13), while pH=2-9 precursors are all amorphous mass. The phase selectivity conforms to the complicated solution chemistries of lanthanum cation and niobate. Like vanadate, tungstate and molybdate, niobate undergoes strong polymerization and protonation to $Nb_6O_{19-z}(OH)_z^{(8-z)-}$ polyoxoniobates in solution, which may simultaneously dissociate to form polyoxoanions of $[Nb_{12}O_{36}]^{12-}$ for pH=4-7, $[Nb_{10}O_{28}]^{6-}$ for pH=5.5-10.8, and $[Nb_6O_{19}]^{8-}$ at sufficient alkalinity (pH≥11) [21-23]. Another indispensable consideration is the hydrolysis of La^{3+} to $[La(OH)_x(NO_3)_y(H_2O)_z]^{3-x-y}$ complex under alkaline conditions [21,24]. Increasing solution pH promoted hydrolysis to yield more OH^- (larger x) and less NO_3^- (smaller y) and also improved reactivity of hydrolyzed La species, ultimately led to direct precipitate as $La(OH)_3$. Hence, the free $[Nb_{10}O_{28}]^{6-}$ and $[Nb_6O_{19}]^{8-}$ species showed the limited reactivity towards La species to produce $LaNb_5O_{14}$. XRD analysis of the precursors after calcination at 900 ºC (Fig. 1) illustrated that the amorphous precursors at pH=2 and 3 directly transformed into o-Nb_2O_5 (JCPDS No. 00-019-0862) and o-$LaNb_5O_{14}$, and pH=4 and 5 ones exclusively yielded o-$LaNb_5O_{14}$. The targeted monoclinic-structured (m-) $LaNbO_4$ (JCPDS No. 01-083-1911) may be crystallized up to solution pH≥6, and becomes the only one at pH = 8-13. The above results further manifested hydrothermal products contain the amorphous mass of lanthanum cations

and niobate. Furthermore, increasing solution pH led to more split and sharper (-121) and (121) diffraction peaks, implying a higher crystallinity and/or larger crystallite size of the product. It is noteworthy that solution pH of 11 unexpectedly weakened the whole diffraction peaks, which may be related to the quantitative transformation from $[Nb_{10}O_{28}]^{6-}$ to $[Nb_6O_{19}]^{8-}$ [22].

The lattice framework of fergusonite-type m-$LaNbO_4$ (space group: *I*2/*c*) based on the data of structural refinement is depicted in Fig. S2 [25]. The unit cell is composed of distorted LaO8 dodecahedron (six) and NbO6 octahedron (six), and both La and Nb reside at the 4e sites of *C*2 symmetry. Each of LaO8 are linked with adjacent NbO6 (or LaO8) by edge-sharing to form zig-zag chains. There are two types of coordinating oxygen atoms of O1 and O2, with four O1 (O1′ crystallographically equivalent to O1) and four O2 (O2′ equivalent to O2) for LaO8, and four O1 and two O2 for NbO6. La-O1 bond length is fairly close to La-O1′ one, while the bond length of La-O2 is remarkable larger that of La-O2′, the similar situation can be observed for Nb-O1/ Nb-O1′ bond length. As a result, LaO8 dodecahedron are interlinked in the whole 3D crystallographic direction, and simultaneously isolate 1D zig-zag chain of NbO6 octahedron. Rietveld refinement of the XRD pattern for the pH=10 $LaNbO_4$ after calcination at 900 ºC using the existing crystallographic data of $LaNbO_4$ as initial model yielded acceptable reliability factors (R_{wp}=10.107%, R_p=7.56%, χ^2=3.68) (Fig. S3).

FE-SEM observation of the hydrothermal products (Fig. S4) revealed that solution pH significantly affects coordination chemistry and ionic mobility [26], and thus results in the multiform morphologies of poorly-crystallized granular agglomerates (~50 nm;

pH=2-5 and 9, Fig. S4a-d and h), mixed shapes of microplate-like assemblies (lateral size ~1-1.5 μm, thickness ~50 nm) and granular agglomerates (~50 nm) (pH=6-8, Fig. S4e-g), and microbelt-like assemblies (length ~1-3 μm, width up to ~500 nm) of rounded nanoparticles (~50 nm) and/or nanorods (length ~0.2-1 μm) (pH=10-13, Fig. S4i-l). For pH=10-13 samples, raising pH promoted the one-dimensional growth to yield a mass of discrete nanorods and microbelts.

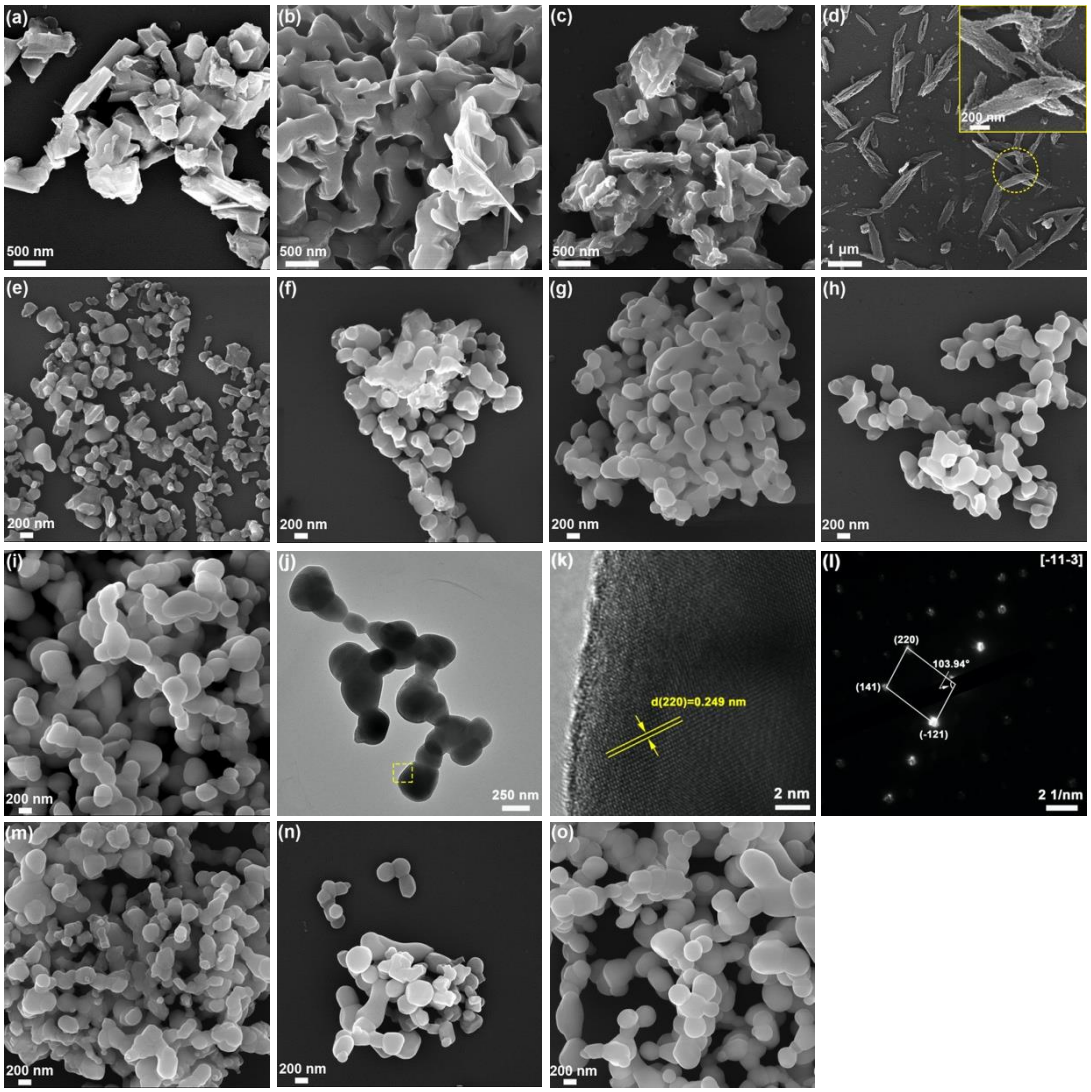

Fig. 2 FE-SEM (a-i and m-o) and TEM (j) morphologies for the products hydrothermally synthesized under pH 2 (a), 3 (b), 4 (c), 5 (d), 6 (e), 7 (f), 8 (g), 9 (h), 10 (i and j), 11 (m), 12 (n) and 13 (o) after calcination at 900 ºC. The insets in (d) and (f) are for magnified views. Part (k) and (l) show the HR-TEM lattice fringes and SAED patterns of the pH=10 one.

Apart from the changes of phase composition, calcination collapsed the shapes and facilitated the inter-crystallite sintering to the extent (Fig. 2). SEM and TEM morphologies (Fig. 2i and j) demonstrated that $LaNbO_4$ obtained under pH=10 consists of agglomerates interconnected with well-defined nanoparticles (~200-500 nm). High-resolution TEM analysis (HR-TEM, Fig. 2k) taken from the rectangle region in Fig. 2j better resolved the lattice fringes with interplanar spacing of ~0.249 nm, which well correspond to the (220) plane of monoclinic $LaNbO_4$ (JCPDS No. 01-083-1911: d_{220}=0.25045 nm). Selected-area electron diffraction (SAED, Fig. 2l) pattern yielded a series of well-arranged spots which can be indexed to (220), (141) and (-121) planes, and the measured dihedral angle of ~103.94º for (220)/(-121) planes approximately coincides with the calculated value of 104.04º. The results also confirmed single crystalline nature of an individual nanoparticulate.

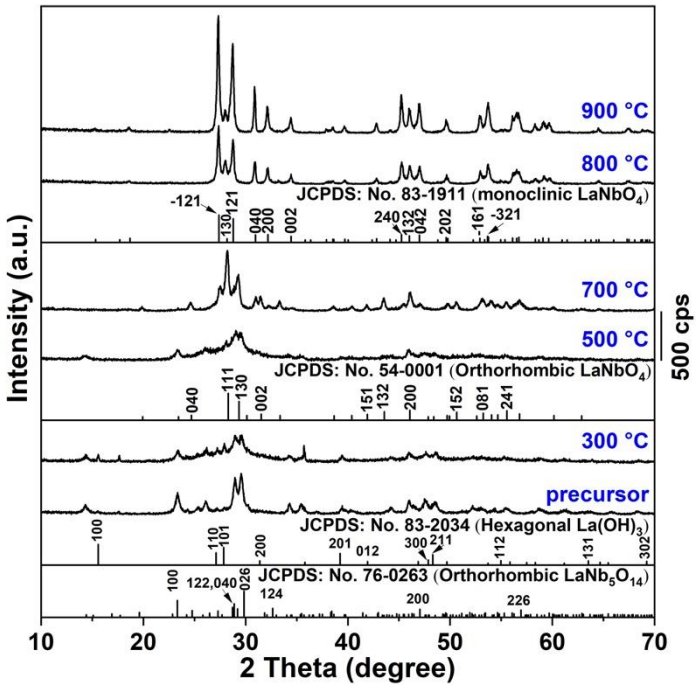

Fig. 3 XRD profiles for the hydrothermally crystallized pH=10 precursor before and after

calcination at different temperatures with a holding period of 2 h.

Fig. 3 investigated calcination kinetic process of as-synthesized pH=10 precursor, where a phase mixture of $La(OH)_3$ and $LaNb_5O_{14}$ can be retained up to 300 ºC. Annealing at 500 ºC additionally hastened the chemical reaction of h-$La(OH)_3$ and o-$LaNb_5O_{14}$ ($2La(OH)_3 + LaNb_5O_{14} = 5LaNbO_4 + 6H_2O$) to yield trace orthorhombic (o-) $LaNbO_4$ (JCPDS No. 00-054-0001). Elevating the temperature to 700 ºC accelerated the generation of o-$LaNbO_4$ (major), and also induced a phase transformation from poorly crystallized o-$LaNbO_4$ to m-$LaNbO_4$ (minor), with the latter being single phase up to 800 ºC. Calcining at even higher temperature of 900 ºC caused no changes to the monoclinic crystal structure, but obviously strengthened the diffractions of m-$LaNbO_4$. Previous studies demonstrated that high-temperature calcination facilitated luminescence by eliminating quenching defects such as surface dangling bonds [27]. TG/DSC curves of pH=10 precursor includes two major stages of weight loss up to ~800 ºC (Fig. S5). The first stage (~1.41% up to 370 ºC) accompanied by a endothermic peak at ~318 ºC is ascribed to the removal of surface adsorption water and intermolecular hydration water in $La(OH)_3$. The second stage (~0.66%) within the ~370-700 ºC temperature range and an endothermic peak at 539 ºC may be derived from the formation of o-$LaNbO_4$ via o → m phase transition. SEM observation (Fig. 4) found that microbelt-like architectures (Fig. 4a and b) disintegrated into loosely-agglomerated nanorods (Fig. 4c and d), and eventually into nanoparticles (~200 and 500 nm, Fig. 4e and f). In contrast, phase-pure $LaNbO_4$ can only be crystallized via

solely high-temperature solid-state reaction at 1200 ºC for 6 h, and its crystallinity is inferior to that of pH=10 one. The as-obtained rough aggregates (~2-3 μm sized irregular objects) with inter-crystallite sintering (Fig. S6) are detrimental to photoluminescence when compared with calcination-assisted hydrothermal nanocrystallites. This may be owning to the more surface/structural defects and less RE^{3+} located at/near crystallite surface, and thus led to the for scattering and quenching of excitation light [28]. Huang et al. compared the photoluminescence properties of $NaLa(WO_4)_2$:0.05Tb^{3+} microspindles and irregular blocks synthesized via hydrothermal process and solid-state reaction, and found that the former exhibits the higher Tb^{3+} emissions owning to the smooth surface [29]. The 800-1000 ºC calcined products are of h-La_2O_3, o-$LaNb_5O_{14}$ and m-$LaNbO_4$, and raising temperature promoted the crystallization of m-$LaNbO_4$.

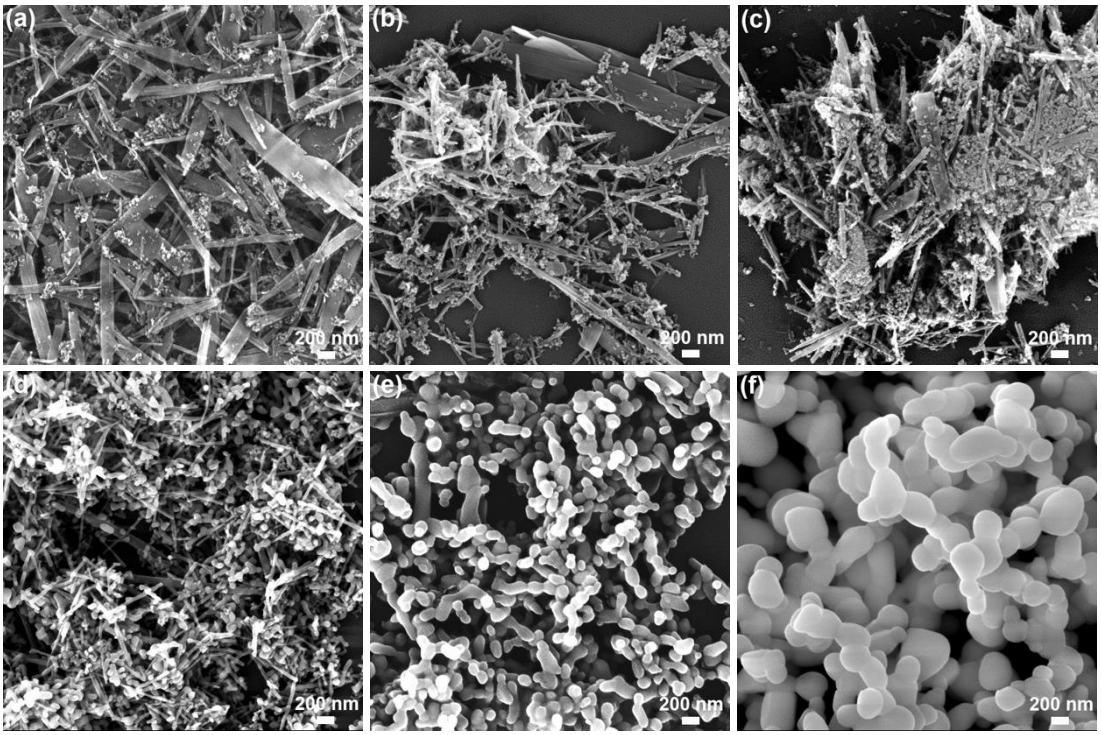

Fig. 4 FE-SEM images for the hydrothermally crystallized pH=10 precursor before (a) and after

calcination at 300 (b), 500 (c), 700 (d), 800 (e) and 900 ºC (f).

The effect of NbO_4^{3-}/La^{3+} molar ratio *R* on phase structure and morphology of the pH=10 product obtained under otherwise identical synthesis conditions was investigated in Fig. S7 and Fig. S8. It is seen that m-$LaNbO_4$ purity can only be retained at *R*=1, while *R*=0.75 one contains m-$LaNbO_4$ and trace La_2O_3 owning to the insufficient La source. For $LaNbO_4$, the relatively low crystallinity and an extraordinarily strong (130) diffraction indicated largely exposure of (130) plane. FE-SEM analysis found that *R*=0.75 product has smaller and uniform-sized granular aggregates (~50-200 nm) when compared with *R*=1 one (Fig. S8a). A slight excess of NbO_4^{3-} at *R*=1.2 prevented o → m phase transformation resulting from kinetic reasons, and ultimately led to the sufficient crystallization of m-$LaNbO_4$ with the weak (-121) and (121) diffractions and the appearance of o-$LaNbO_4$ and cubic (c-) $La_{0.33}NbO_3$ impurity (JCPDS No. 00-036-0126). Hence, both of short nanorods (~200-400 nm in length, ~50-100 nm in diameter) and nanoparticles (~200-500 nm) were witnessed from the SEM micrographs in Fig. S8c. Superfluous NbO_4^{3-} tends to react with relatively low stoichiometric amount of La^{3+} for more c-$La_{0.33}NbO_3$, and as a consequence, the strong diffractions of c-$La_{0.33}NbO_3$ and almost vanished diffractions of large-sized m-$LaNbO_4$ particulates and h-La_2O_3 were the result up to *R*=4 (Fig. S8g).

3.2 Photoluminescence of $LaNbO_4:Yb^{3+},Eu^{3+}$ nanophosphors

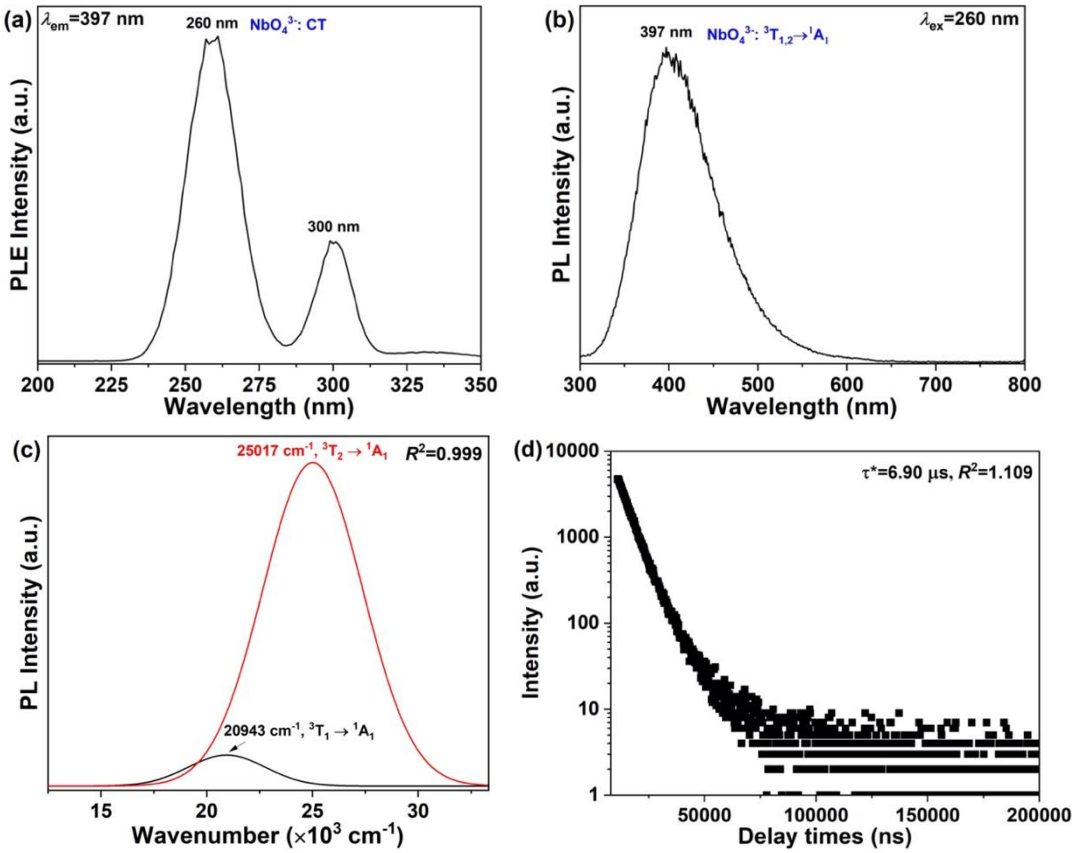

Fig. 5 Photoluminescence excitation (PLE, a) and photoluminescence (PL, b) spectra of $LaNbO_4$ phosphors synthesized by calcining the pH=10 precursor at 900 ºC for 2 h. Part (c) shows deconvolution of the ~397 nm emission by Gaussian fitting. Part (d) is semi-log plot of fluorescence decay for the 460 nm emission of NbO_4^{3-} in $LaNbO_4$.

Fig. 5a-c present the photoluminescence excitation (PLE) and emission (PL) of $LaNbO_4$ phosphor obtained through calcining the pH=10 precursor at 900 ºC. It is thus clear that PLE spectrum has two well-separated and broad sub-bands centered at 260 and 300 nm separately corresponding to the parity-allowed $^1A_1 \rightarrow {}^1T_2$ and $^1A_1 \rightarrow {}^1T_1$ transitions from $O^{2-} \rightarrow Nb^{5+}$ charge transfer (CT) within the NbO_4^{3-} ligand in terms of ligand field theory, where $^1A_1 \rightarrow {}^1T_2$ belongs to spin-allowed electric-diople transition, while $^1A_1 \rightarrow {}^1T_1$ transition will be enhanced with increasing deviation from a cubic symmetry [30]. Exciting the $LaNbO_4$ phosphor with the dominant 260 nm UV light produced a broad emission peaked at 397 nm, which is assignable to the intrinsic

emission of distorted NbO_4^{3-}. Gaussian deconvolution of the asymmetric PL band gave two overlapping peaks located at 20943 and 25017 cm^{-1}, which is originated from intrinsic $^3T_2 \rightarrow {}^1A_1$ and $^3T_1 \rightarrow {}^1A_1$ transitions via radiative decay, respectively. Fluorescence decay kinetics for the 397 nm emission of NbO_4^{3-} can be well-fitted by a bi-exponential equation as $I(t) = A_1\exp(-t/\tau_1) + A_2\exp(-t/\tau_2) + C$ (Fig. 5d), where $I(t)$ is the emission intensity at time t, τ_1 and τ_2 denote exponential components of the decay times, and A_1, A_2 and C are constants, and the average lifetime can be determined by the function $\tau^* = (A_1\tau_1^2 + A_2\tau_2^2)/(A_1\tau_1 + A_2\tau_2)$ being ~6.90 μs [31].

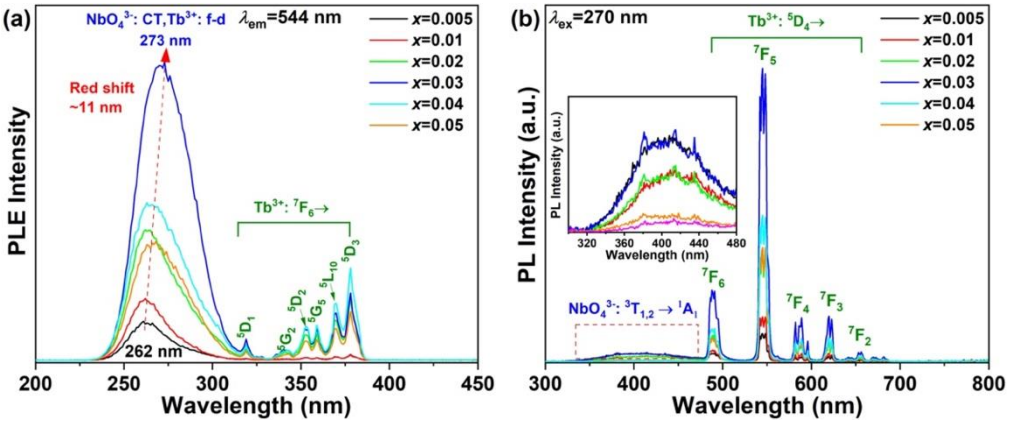

Fig. 6 PLE (a) and PL (b) spectra for the 900 ºC calcined $LaNbO_4$:$x$$Tb^{3+}$ (x=0.005-0.05) phosphors.

The luminescence behaviors of the calcined $LaNbO_4$:Tb^{3+} phosphors (x=0-0.05) synthesized under the identical condition of the aforesaid $LaNbO_4$ phosphor were discussed as follows to elaborate the energy interaction mechanism between RE^{3+} and NbO_4^{3-} host. XRD profiles of $LaNbO_4$:$x$$Tb^{3+}$ products (x=0-0.05) synthesized under the identical condition of pH=10 sample (Fig. S9) testified that single-phased m-$LaNbO_4$ can only be retained up to x=0.03. Further increasing Tb^{3+} concentration to 4 at% additionally produced tetragonal (t-) $LaNbO_4$ (JCPDS No. 00-050-0919; space group: $I4_1/a$) [32], as demonstrated by the appearance of (200) and extraordinarily strong (112) diffractions in the t-$LaNbO_4$ standard (JCPDS No. 00-050-0919), implying the change

of crystallization habit. Such a sequence phase transition of m → t-$LaNbO_4$ commonly occurred at high temperature in the range of ~490-525 ºC [33]. However, this phenomenon observed in our results could be due to more distorted crystal structure by smaller Tb^{3+}, which further affected sintering kinetics, though yet needs further clarification. It is also evident that Tb^{3+} incorporation weakened and broadened the diffractions, and meanwhile gradually drifts the (040) and (200) diffractions toward larger angle side by ~0.22º and 0.24º, respectively. This complies with the fact that smaller Tb^{3+} ions would substitute larger La^{3+} ($r_{Tb^{3+}}$=1.04 Å, $r_{La^{3+}}$=1.16 Å under 8-fold coordination (CN=8)) to occupy asymmetric C_{2h}^6 of m-$LaNbO_4$ and/or C_{4h}^6 sites of t-$LaNbO_4$ without an inversion center owning to lanthanide contraction, and thus enlarged the interplanar spacing [34,35]. Monitoring at 544 nm green emission of Tb^{3+} produced a broad and strong band in the ~200-315 nm spectral region by O^{2-} → Nb^{5+} CT in NbO_4^{3-} overlapped with spin-allowed interconfigurational $4f^8$ → $4f^7d^1$ of Tb^{3+} and intra-$4f^8$ narrow-band transitions of Tb^{3+} (Fig. 6a). The excitation intensities of NbO_4^{3-} and Tb^{3+} were found to be remarkably enhanced by increasing Tb^{3+} contents, which also resulted in an appreciable red-shift from 262 nm to 273 nm. This is primarily attributed to a stronger energy transfer (ET) of CTB of NbO_4^{3-} with f-d and/or 4f states of Tb^{3+} via resonant interaction, more distorted NbO_6 octahedron caused by short Tb-O bond and stronger f-d transition of Tb^{3+}. Upon UV excitation at 270 nm, PL spectra exhibit two components, that is, negligibly weak self-activated broad-band emission of NbO_4^{3-} in the ~300-475 nm region and characteristic $^5D_4$ → ^7F_J (J=2-6) transition of Tb^{3+} at ~488 nm (J=6), 544 nm (J=5), 589 nm (J=4), 620 nm (J=3) and 656 nm (J=2) (Fig. 6b). Tb^{3+} doping did not bring about any change of peak position, but drastically deteriorated the NbO_4^{3-} emission, further verified the efficient NbO_4^{3-} → Tb^{3+} ET. The

best luminescent $LaNbO_4$:0.03Tb^{3+} phosphor presents integral intensities ~10 times than $LaNbO_4$:0.005Tb^{3+} counterpart for the dominant ~544 nm green emission. Accordingly, the optimal Tb^{3+} content is 3 at% due to the localized concentration quenching, which has been designated as the initial Tb^{3+} content to accomplish luminescence tailoring and enhancement by codoping of Eu^{3+}.

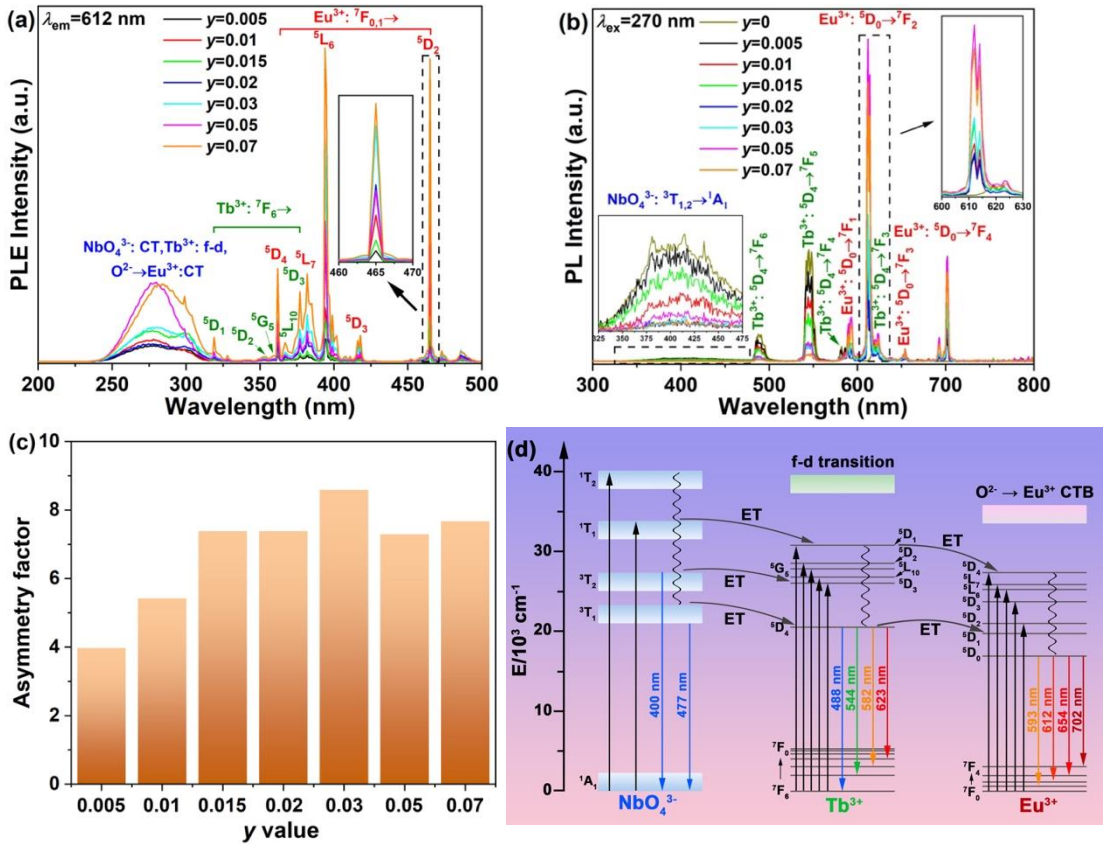

Fig. 7 PLE (λ_{em}=612 nm, a) and PL (λ_{ex}=270 nm, b) spectra for the $LaNbO_4$:0.03Tb^{3+},yEu^{3+} (y=0.005-0.07) phosphors after calcination at 900 ºC. Part (c) plots the asymmetry factor of luminescence against the Eu^{3+} contents. Part (d) is a schematic diagram showing the excitation, emission and possible NbO_4^{3-} → Tb^{3+} → Eu^{3+}energy transfer processes.

XRD analysis of $LaNbO_4$:0.03Tb^{3+},yEu^{3+} (y=0-0.07, Fig. S10) indicated a pure m-$LaNbO_4$ for y=0-0.03, a phase mixture of m- and t-$LaNbO_4$ for y=0.05 and 0.07, and ~0.04 and 0.08° right-shift as shown by an amplified view of the diffractions at 2θ=30.5-32.5° due to size difference ($r_{Eu^{3+}}$=1.066 Å, CN=8). Fig. 7a and b shows the PLE and PL spectra of ternary $LaNbO_4$:Tb^{3+},Eu^{3+} phosphors. In each case, PLE spectra

contain a broad excitation of $O^{2-} \rightarrow Nb^{5+}$ CT, $O^{2-} \rightarrow Eu^{3+}$ CT and $4f^8 \rightarrow 4f^7d^1$ transition of Tb^{3+} by monitoring the $^5D_0 \rightarrow {}^7F_2$ transition of Eu^{3+} at 612 nm, which is hardly distinguished owning to apparent spectral overlap. Besides the relatively weak intra-$4f^8$ transitions of Tb^{3+}, the strong intra-$4f^6$ excitations of Eu^{3+} are also identified at 362 nm ($^7F_{0,1} \rightarrow {}^5D_4$), 382 nm ($^7F_{0,1} \rightarrow {}^5L_7$), 394 nm ($^7F_{0,1} \rightarrow {}^5L_6$), 428 nm ($^7F_{0,1} \rightarrow {}^5D_3$) and 465 nm ($^7F_{0,1} \rightarrow {}^5D_2$). The PL spectra taken under 270 nm excitation of NbO_4^{3-} disclosed the luminescent characteristic of NbO_4^{3-}, Tb^{3+} and Eu^{3+}, and have the strong $^5D_0 \rightarrow {}^7F_2$ electric dipole transition of Eu^{3+} instead of the $^5D_0 \rightarrow {}^7F_1$ magnetic dipole allowed transition, since Eu^{3+} ions reside an asymmetric C_{2h}^6 site without inversion center in terms of Judd-Ofelt theory [36]. It can be inferred from the spectral overlap between NbO_4^{3-} excitation and RE^{3+} emission, intense Eu^{3+} and monotonically reduced NbO_4^{3-} and Tb^{3+} emissions that an efficient $NbO_4^{3-} \rightarrow Tb^{3+} \rightarrow Eu^{3+}$ ET successively occurred in the $LaNbO_4:Tb^{3+},Eu^{3+}$ phosphors. Simultaneously, the symmetric tetragonal structure may be more superior to monoclinic structure for more energy interaction of NbO_4^{3-} with RE^{3+}. As a result, both of $LaNbO_4:0.03Tb^{3+},0.05Eu^{3+}$ and $LaNbO_4:0.03Tb^{3+},0.07Eu^{3+}$ phosphors have stronger broad-band excitation and Eu^{3+} emission across the series of counterparts, and their substantially intensity ratio (asymmetry factor of luminescence, *R*) of $^5D_0 \rightarrow {}^7F_2$ to $^5D_0 \rightarrow {}^7F_1$ is lower that of *y*=0.03 counterpart (Fig. 7c).

The cooperative ET mechanism of $NbO_4^{3-} \rightarrow Tb^{3+} \rightarrow Eu^{3+}$ can be reasonable elucidated as below, and an energy level diagram is simplified in Fig. 7d. Upon 270 nm excitation, electrons in $^1A_1$ ground state are jumped to $^1T_2$ and $^1T_1$ excited state of

NbO_4^{3-} groups, followed by non-radiative relaxation (NR) to lower-lying double-split $^3T_2$ and $^3T_1$ excited state and also ET to the neighboring $^5D_1$ higher level of Tb^{3+} via resonant interaction. The $^3T_2$ and $^3T_1$ energies have two destinations: radiative relaxation to the $^1A_1$ ground state to produce 394/440 nm intrinsic blue emissions of NbO_4^{3-} group; ET to $^5D_3$ and $^5D_4$ state of Tb^{3+}, respectively. The electrons in $^5D_1$ and $^5D_3$ of Tb^{3+} then populate into $^5D_4$ energy level of Tb^{3+} via NR, which is followed by ET to adjacent $^5D_4$ (only arising from $^5D_1$ of Tb^{3+}) and $^5D_1$ level of Eu^{3+}. A part of the $^5D_4$ electrons then fall back to ^7F_J (J=3-6) of Tb^{3+} for the observed 623 nm (red), 582 nm (orange), 544 nm (green) and 488 nm (blue) emissions. After directly absorbing the energies from $^5D_4$ and $^5D_1$ of Tb^{3+}, Eu^{3+} electrons nonradiatively relax to lowest-lying $^5D_0$ excited state, and then radiative relaxation to ^7F_J (J=1-4) ground states for the Eu^{3+} emissions. The more matched $^1T_1$ level of NbO_4^{3-} with $^5D_1$ state of Tb^{3+} and $^3T_1$ level of NbO_4^{3-} with $^5D_4$ state of Tb^{3+} suggested that Tb^{3+} serves as a "bridge" for more efficient $NbO_4^{3-} \rightarrow Tb^{3+} \rightarrow Eu^{3+}$ ET, and thus the conspicuously intense Eu^{3+} emissions were the result.

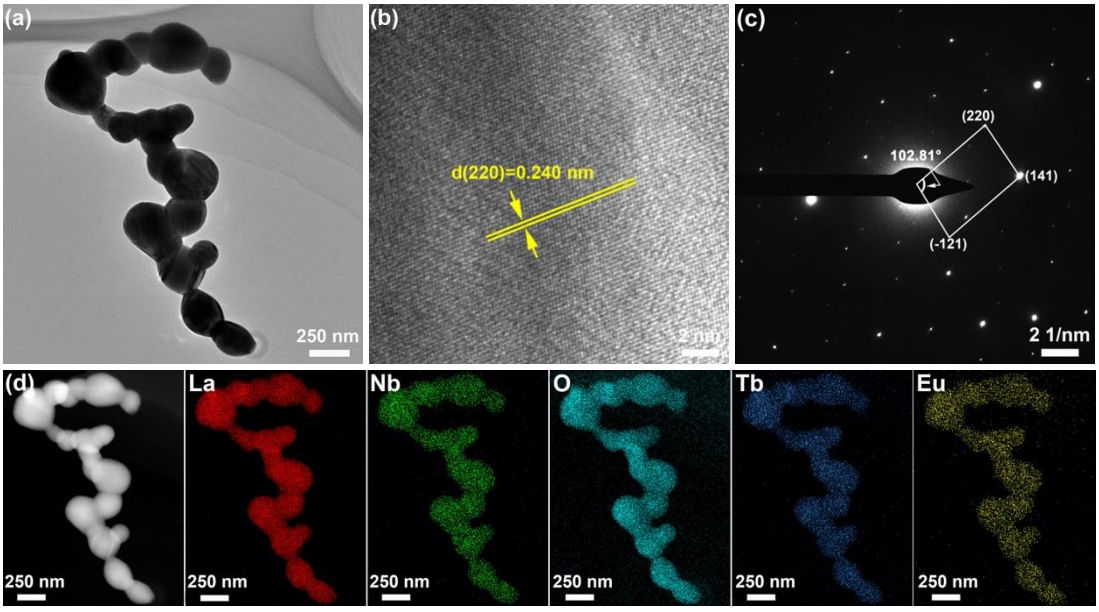

Fig. 8 TEM micrograph (a), HR-TEM lattice fringes (b), SAED pattern (c) and elemental mapping

images (d) taken for the $LaNbO_4$:0.01Tb^{3+},0.01Eu^{3+} phosphor.

In view of the fascinating bluish green emission of $LaNbO_4$:0.01Tb^{3+}, the white light-emitting diode can be attainable through precisely modulating the emission color of $LaNbO_4$:0.01Tb^{3+},*y*Eu^{3+} phosphors (*y*=0-0.02). XRD analysis (Fig. S11) indicated that *y*=0-0.015 products exhibited a phase-pure m-$LaNbO_4$, while concentrated Eu^{3+} up to *y*=0.017-0.02 induced partial crystallization of t-$LaNbO_4$. Moreover, the diffraction intensity of products dramatically decreased when the Eu^{3+} contents exceed 1 at%, and the crystallinity gets better at *y*=0.02 without any obvious peak shifting, which may be caused by the phase transformation and rather limited content of Eu^{3+} in different lattice. With the $LaNbO_4$, $LaNbO_4$:0.01Tb^{3+} and $LaNbO_4$:0.01Tb^{3+},0.01Eu^{3+} for example, analysis of the full-range XRD patterns with the Jade 6.5 software and applying Scherrer formula indeed found that 1 at% Tb^{3+} and 1 at% Eu^{3+} co-substitutions reduced the cell parameter and cell volume (*a*=5.576(2) Å, *b*=11.550(4) Å, *c*=5.212(1) Å, *β*=94.06(4) Å, *V*=334.86 $Å^3$ for $LaNbO_4$; *a*=5.554 (1) Å, *b*=11.536 (3) Å, *c*=5.206(1) Å, *β*=94.03 (3) Å, *V*=332.84 $Å^3$ for $LaNbO_4$:0.01Tb^{3+}; *a*=5.555(1) Å, *b*=11.518(2) Å, *c*=5.195(1) Å, *β*=94.06(2) Å, *V*=331.67 $Å^3$ for $LaNbO_4$:0.01Tb^{3+},0.01Eu^{3+}). Fig. 8 shows the results of TEM for the representative $LaNbO_4$:0.01Tb^{3+},0.01Eu^{3+}, where it is seen that the product comprises ~200-300 nm sized nanoparticles (Fig. 8a). HR-TEM analysis (Fig. 8b) also confirmed the distinct exposure of (220) facet, but codoping of smaller Tb^{3+} and Eu^{3+} slightly reduced d-spacing to be ~0.240 nm. SAED pattern (Fig. 8c) unambiguously identified the diffraction spots arising from (220), (141) and (-121), and the dihedral angle of (220)/(-121) planes decreased to ~102.81º. Elemental

mapping (Fig. 8d) via STEM manifested that La, Nb, O, Tb and Eu elements are homogeneously distributed throughout the whole granular aggregates, which further proved the formation of solid solution.

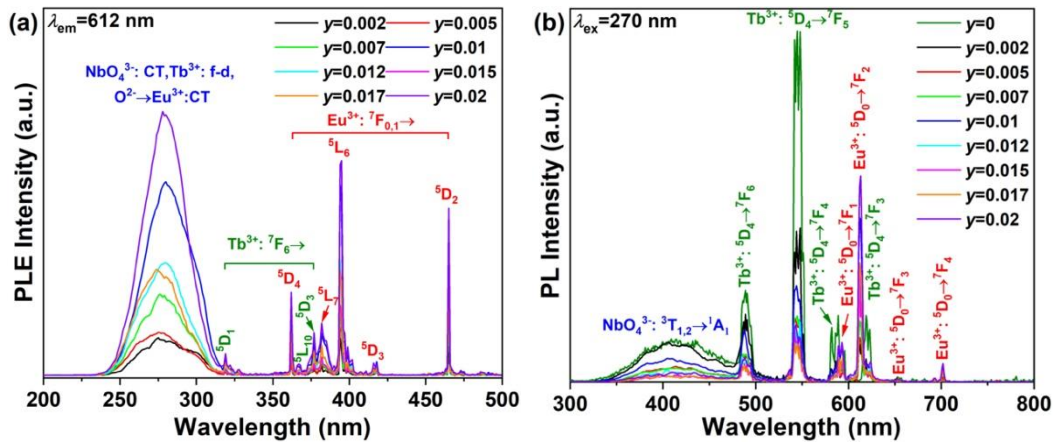

Fig. 9 PLE (λ_{em}=612 nm, a) and PL (λ_{ex}=270 nm, b) spectra for $LaNbO_4$:0.01Tb^{3+},yEu^{3+} (y=0.002-0.02) phosphors.

Fig. 9 shows the PLE and PL spectra for $LaNbO_4$:0.01Tb^{3+},yEu^{3+} (y=0.002-0.02) phosphors. The excitation and emission intensities of Eu^{3+} exclusively increase with the increase in y to 0.01, beyond which the intensity goes down until y=0.017, whereas an opposite trend observed for NbO_4^{3-} and Tb^{3+}. $LaNbO_4$:0.01Tb^{3+},0.02Eu^{3+} phosphor shows the undoubtedly strongest excitation and Eu^{3+} emission, which indicated the favorable resonant ET of NbO_4^{3-} → Tb^{3+} → Eu^{3+}. The above result also illustrates the quenching concentration of Eu^{3+} in m-$LaNbO_4$ is determined to be ~1 at%, and tetragonal lattice favors the photoluminescence. The Commission international de l´éclairage (CIE) chromaticity diagram (Fig. 10) and CIE coordinates (Table S1) exhibits full-visible-spectrum emitting $LaNbO_4$:xTb^{3+},yEu^{3+} phosphors including deep blue (x=0, y=0), deep green (x=0.05, y=0), white (x=0.01, y=0.01) and deep red (x=0.03, y=0.07) regions, which is in good accordance with the vivid multicolor luminescence

of the phosphors under 254 nm UV irradiation from a hand-held UV lamp. The red and white light-emitting $LaNbO_4:0.03Tb^{3+},0.05Eu^{3+}$ and $LaNbO_4:0.01Tb^{3+},0.01Eu^{3+}$ phosphors were calculated to have absolute quantum efficiencies of 20.43% and 33.07%, respectively.

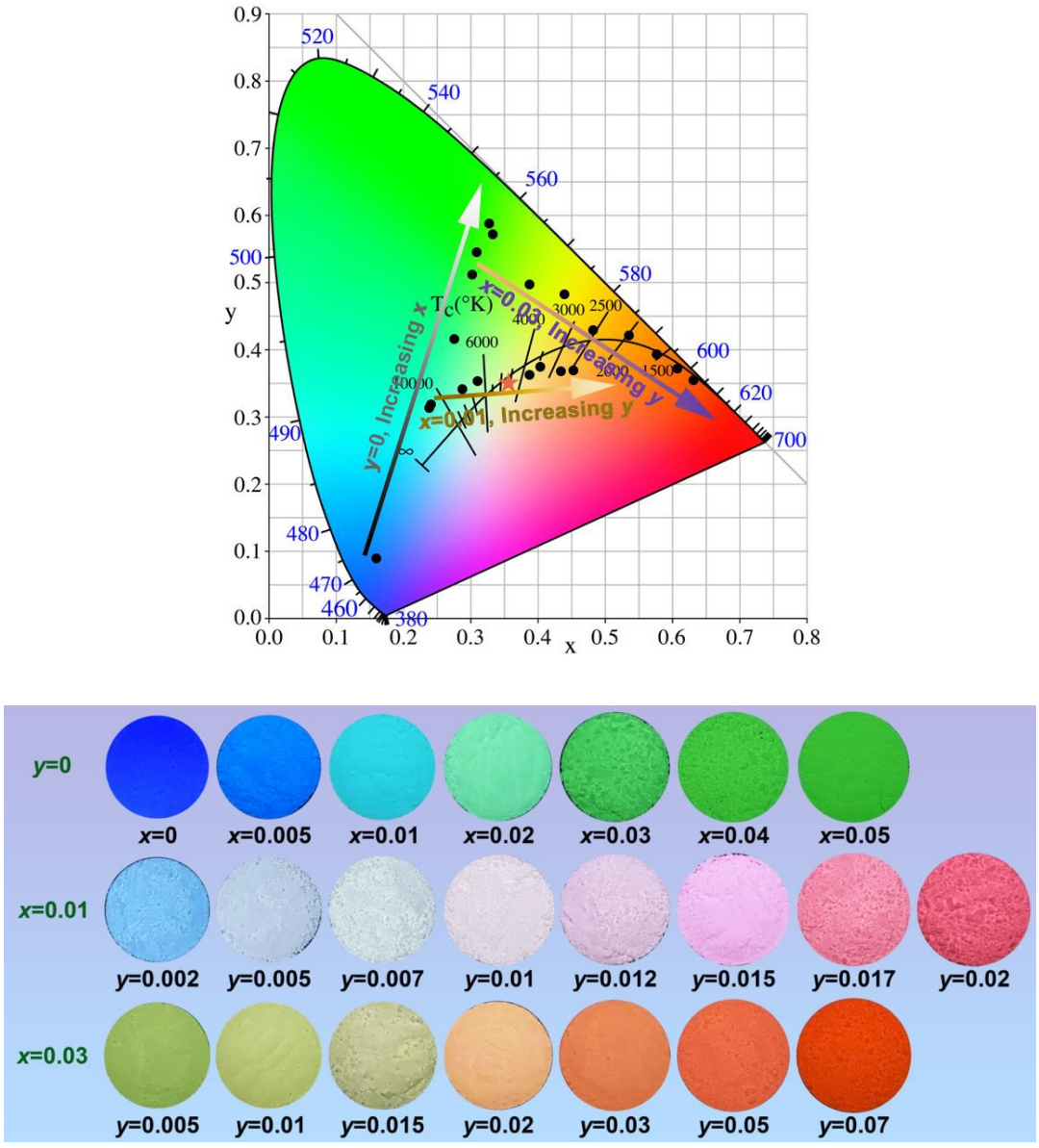

Fig. 10 CIE chromaticity diagram (upper) and appearances of multicolor luminescence under a 254 nm UV lamp irradiation (bottom) of $LaNbO_4:xTb^{3+}$ (x=0-0.05), $LaNbO_4:0.01Tb^{3+},yEu^{3+}$ (y=0.002-0.02) and $LaNbO_4:0.03Tb^{3+},yEu^{3+}$ (y=0.005-0.07) phosphors.

3.3 Thermal stability and UV-excited pc-WLEDs performance of $LaNbO_4:0.01Tb^{3+},0.01Eu^{3+}$

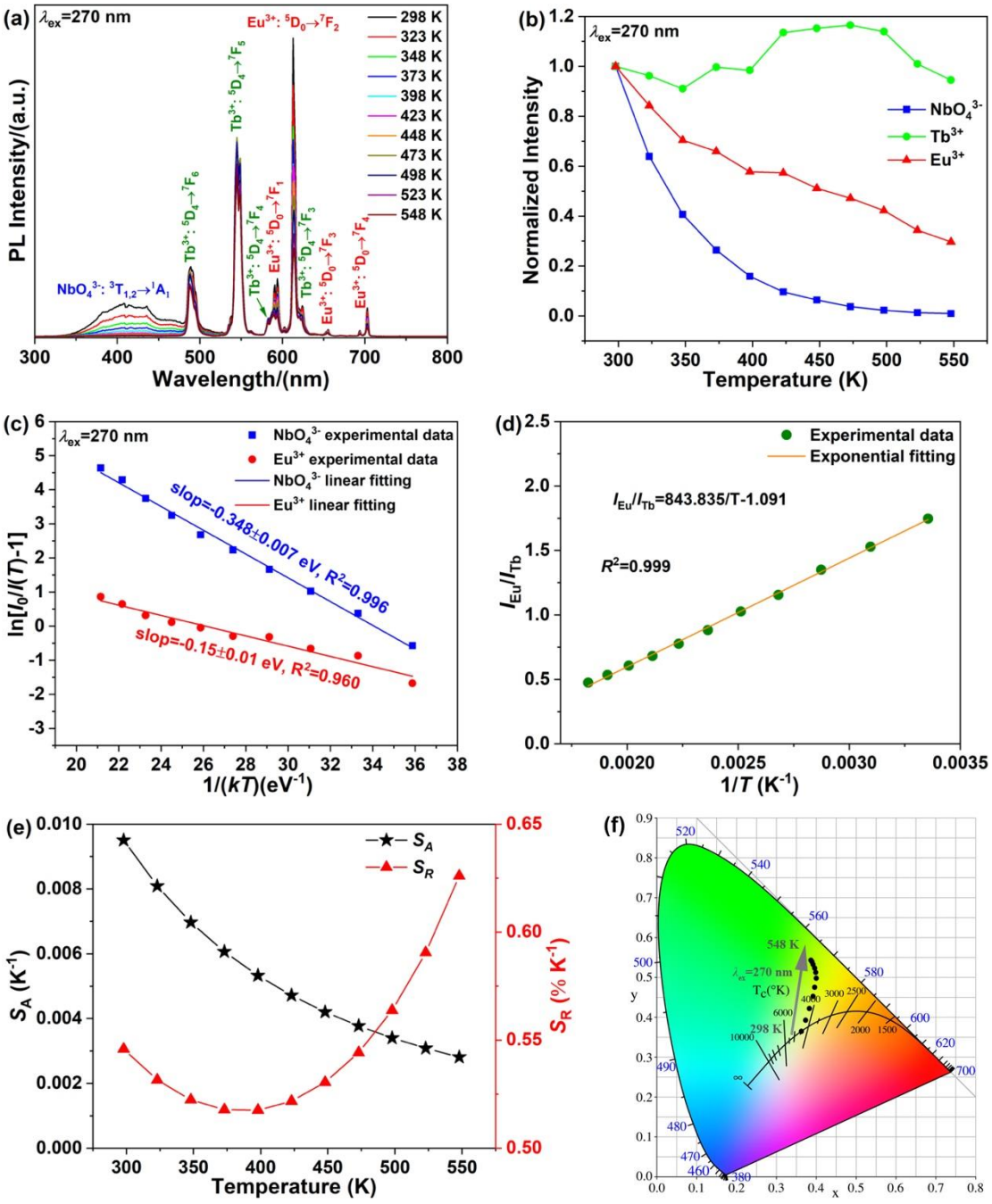

Fig. 11 Temperature-dependent emission spectra (a), the normalized emission intensity of NbO_4^{3-}, Tb^{3+} and Eu^{3+} (b) and the $\ln[I_0/I(T)\text{-}1]$ *versus* $1/(kT)$ plot (c) for $LaNbO_4:0.01Tb^{3+},0.01Eu^{3+}$ phosphor under 270 nm excitation within 298-548 K. Parts (d-f) show the FIR (I_{Eu}/I_{Tb}), absolute sensitivity (S_a) and relative sensitivity (S_r), CIE chromaticity diagram for the temperature-course luminescence of $LaNbO_4:0.01Tb^{3+},0.01Eu^{3+}$ phosphor under 270 nm excitation, respectively.

Phosphor is rather susceptible to surrounding environment temperature, and

thereby, the thermal quenching behavior is essential for thermal stability in WLED applications. Herein, the temperature-dependent luminescence of $LaNbO_4$:0.01Tb^{3+},0.01Eu^{3+} phosphor was investigated in the range of 298-548 K (Fig. 11a). Raising temperature did not cause Stokes shift, but rapidly weakened the integral emission intensity of Eu^{3+} and especially NbO_4^{3-}, which can only maintain ~57% and 10% of its initial value at 423 K (Fig. 11b). It is well-documented that the luminescence thermal quenching was caused by a strong electron-phonon coupling and thermally activated crossover process between the excited state and ground state [37-39]. Nevertheless, Tb^{3+} emission was extraordinarily intensified by ~20% at 423 K and then slowly dropped down to 90%, which may be due to the rapidly thermal quenching of NbO_4^{3-} emissions and strong thermal coupling effect by resonant $NbO_4^{3-} \rightarrow Tb^{3+}$ ET toward temperature increment [40]. The quenching activation energy (ΔE) for NbO_4^{3-} and Eu^{3+} luminescence can be assayed from the following Arrhenius equation [41,42]:

$$\ln\left[\frac{I_0}{I(T)}-1\right]=\ln A-\frac{\Delta E}{kT} \quad (1)$$

Where I_0 and $I(T)$ denote the PL intensities at 298 K and absolute temperature T, respectively. A and k are separately a pre-exponential constant and Boltzmann constant of 8.617×10^{-5} eV/K. Fig. 11c shows the plot of $\ln[I_0/I(T)-1]$ *versus* $1/(kT)$ plot. ΔE is thus calculated by the slope of the linear fitting to be ~0.348±0.007 eV for NbO_4^{3-} and 0.15±0.01 eV for Eu^{3+}. Consequently, it is plausible to speculate that $LaNbO_4$:0.01Tb^{3+},Eu^{3+} phosphor is a promising candidate for optical thermometers, among which Tb^{3+} can be employed as a built-in calibration signal to prevent environmental effect, while NbO_4^{3-} and Eu^{3+} with thermal quenching is considered as a temperature detection [43]. Fig. 11d depicted temperature-dependent fluorescence

intensity ratio (abbreviated as FIR) between Eu^{3+}: $^5D_0 \rightarrow {}^7F_2$ (I_{Eu}) and Tb^{3+}: $^5D_4 \rightarrow {}^7F_5$ (I_{Tb}). FIR (I_{Eu}/I_{Tb}) monotonously dropped upon elevating the temperature, and the experimental results are well-fitted with the linear function as FIR (I_{Eu}/I_{Tb})=843.835/T-1.091, implying an attractive luminescent thermometer applied for temperature sensing. The absolute (S_A) and relative (S_R) sensitivities can be expressed as follows against temperature to evaluate the performance of temperature sensing [42].

$$S_A = \left| \frac{d(\mathrm{FIR})}{d(T)} \right| \tag{2}$$

$$S_R = \left| \frac{d(\mathrm{FIR})}{d(T)} \frac{1}{\mathrm{FIR}} \right| \times 100\% \tag{3}$$

It is observed that the maximum values of S_A and S_R are ~0.01 K^{-1} (at 298 K) and 0.63% K^{-1} (at 548 K), respectively, and the former is higher than ~0.0046 and 0.0073 K^{-1} for $NaYF_4:Ce^{3+},Tb^{3+},Eu^{3+}$ and $YNbO_4:Yb^{3+},Er^{3+}$ microcrystals, respectively [44,45]. CIE chromaticity diagram (Fig. 11f) for the $LaNbO_4:0.01Tb^{3+},0.01Eu^{3+}$ phosphor found that the luminescent colors shift from white to yellowish green under 270 nm excitation, which is associated with the weakened NbO_4^{3-} (major) and Eu^{3+} (minor) emissions and almost insusceptible Tb^{3+} emissions.

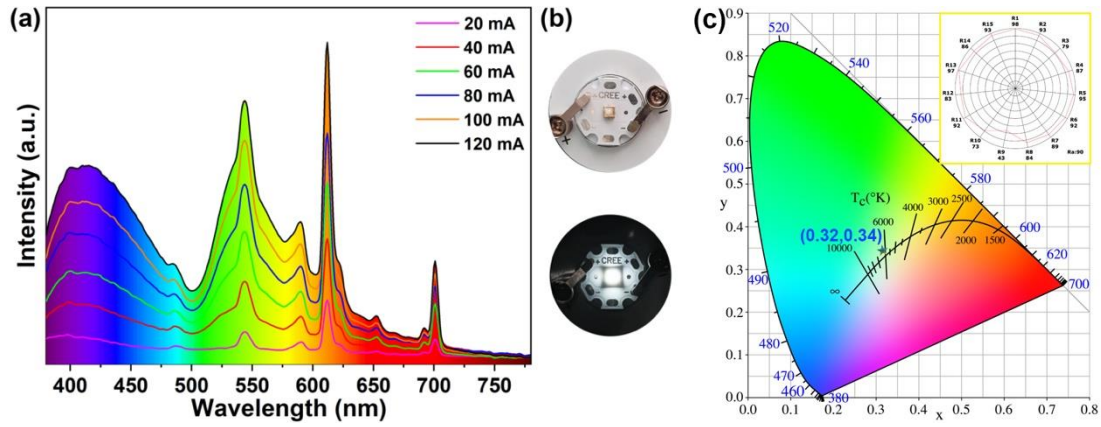

Fig. 12 The electroluminescence spectra of 275 nm pumped WLED via combining with the $LaNbO_4:0.01Tb^{3+},0.01Eu^{3+}$ phosphor under 20-120 mA current driving (a), the appearances of the WLED device with the current on and off (b), CIE chromaticity diagram (c) for the as-fabricated WLED lamp under 20 mA driving. The inset in (c) shows color rendering index *R*a and R1-R15 factors.

The as-fabricated $LaNbO_4$:0.01Tb^{3+},0.01Eu^{3+} phosphor was embedded on a commercial 275 nm deep UV chip to integrate a pc-WLED device. The characteristics of electroluminescence spectra (Fig. 12a) are almost identical to PL spectrum of $LaNbO_4$:0.01Tb^{3+},0.01Eu^{3+} (Fig. 9b) without considering the change of driving current. The white-emitting intensity continuously increased when the driving current increased from 20 to 120 mA. The CIE coordinate of around (0.32, 0.34) is close to ideal white light of (0.33, 0.33), and the CCT of ~5694 K and CRI value of ~90 under current of 20 mA are more beneficial than the commercial YAG:Ce^{3+} (CCT~7750 K, CRI<75.0) (Fig. 12c), and obtained prospective *R* parameters (*R*1-*R*15) [46].

4. Conclusion

The full-color emitting $LaNbO_4$:*x*Tb^{3+},*y*Eu^{3+} (*x*=0-0.05, *y*=0-0.07) phosphors were crystallized at 24 h of hydrothermal reaction at 200 ºC and pH=10 after calcination at 900 ºC. Phase composition and morphology analyses demonstrated that calcining the pH=10 precursor at 500 ºC induced the formation of orthorhombic $LaNbO_4$, and the 800 ºC calcined products exclusively crystallized in monoclinic structure. Superfluous Tb^{3+} and Eu^{3+} additionally induced a phase transition from monoclinic to tetragonal $LaNbO_4$. Upon 270 nm excitation, the $LaNbO_4$: Tb^{3+},Eu^{3+} phosphors showed the blue NbO_4^{3-}, green Tb^{3+} and red Eu^{3+} emissions. Codoping of 0.01Tb^{3+} and 0.01Eu^{3+} produced warm white emission with desired color coordinates of (0.36,0.35), and also exhibited favorable resistance to thermal quenching with activation energy of NbO_4^{3-} and Eu^{3+} being ~0.348±0.007 eV and 0.15±0.01 eV, respectively. Combining white-emitting $LaNbO_4$:0.01Tb^{3+},0.01Eu^{3+} with deep UV chip for a single-component pc-WLED device exhibited ~5684 K and 90 of correlated color temperature and color rendering index, respectively.

Declaration of Competing Interest

The authors declared that there is no conflict of interest.

Acknowledgements

This work was supported in part by the Doctoral Start-up Foundation of Liaoning Province (Grant No. 2022-BS-311).

References

[1] G.G. Li, Y. Tian, Y. Zhao, J. Lin, Recent progress in luminescence tuning of Ce^{3+} and Eu^{2+}-activated phosphors for pc-WLEDs, Chem. Soc. Rev. 44 (2015) 8688-8713.

[2] M.H. Fang, Z. Bao, W.T. Huang, R.S. Liu, Evolutionary generation of phosphor materials and their progress in future applications for light-emitting diodes, Chem. Rev. 122 (2022) 11474-11513.

[3] A. Bindhu, J.I. Naseemabeevi, S. Ganesanpotti, Distortion and energy transfer assisted tunability in garnet phosphors, Crit. Rev. Solid State 47 (2022) 621-664.

[4] D.J. Liu, X.H. Yun, P.P. Dang, H.Z. Lian, M.M. Shang, G.G. Li, J. Lin, Yellow/orange-emitting $ABZn_2Ga_2O_7:Bi^{3+}$ (A = Ca, Sr; B = Ba, Sr) phosphors: optical temperature sensing and white light-emitting diode applications, Chem. Mater. 32 (2020) 3065-3077.

[5] S.X. Li, Y.H. Xia, M. Amachraa, N.T. Hung, Z.B. Wang, S.P. Ong, R.-J. Xie, Data-driven discovery of full-visible-spectrum phosphor, Chem. Mater. 31 (2019) 6286-6294.

[6] P.P. Dang, D.J. Liu, G.G. Li, A.A. Al Kheraif, J. Lin, Recent advances in bismuth

ion-doped phosphor materials: Structure design, tunable photoluminescence properties, and application in white LEDs, Adv. Optical Mater. 8 (2020) 1901993.

[7] C.Y. Wang, T. Takeda, O.M. ten Kate, S. Funahashi, R.-J. Xie, K. Takahashi, N. Hirosaki, New deep-blue-emitting Ce-doped $A_{4-m}B_nC_{19+2m}X_{29+m}$ (A = Sr, La; B = Li; C = Si, Al; X = O, N; $0\leq m\leq 1$; $0\leq n\leq 1$) phosphors for high-color-rendering warm white light-emitting diodes, ACS Appl. Mater. Interfaces 11 (2019) 29047-29055.

[8] M.M. Shang, C.X. Li, J. Lin, How to produce white light in a single-phase host? Chem. Soc. Rev. 43 (2014) 1372-1386.

[9] M.T. Li, J.-G. Li, Extensive tailoring of $REPO_4$ and $REVO_4$ crystallites via solution processing and luminescence, CrystEngComm 24 (2022) 4841-4852.

[10] Z.H. Wang, Y.M. Li, Q. Zhu, X.J. Wang, M.Y. Liao, Hydrothermal crystallization of VO_4^{3-} stabilized t-$Gd(P,V)O_4:Eu^{3+}$ nanocrystals for remarkably improved and color tailorable luminescence, Chem. Eng. J. 357 (2019) 84-93.

[11] K. Li, Y. Zhang, X.J. Li, M.M. Shang, H.Z. Lian, J. Lin, Host-sensitized luminescence in $LaNbO_4:Ln^{3+}$ (Ln^{3+} = Eu^{3+}/Tb^{3+}/Dy^{3+}) with different emission colors, Phys. Chem. Chem. Phys. 17 (2015) 4283-4292.

[12] S.J. Ding, H.T. Zhang, Y.Z. Chen, Q.L. Zhang, R.Q. Dou, W.P. Liu, G.H. Sun, D.L. Sun, Structure, electronic and optical properties of $LaNbO_4$: An experimental and first-principles study, Solid State Commun. 277 (2018) 7-12.

[13] J.Y. Si, N. Yang, M.J. Xu, G.H. Li, G.M. Cai, W. Yi, J. Zhang, Structure and tunable luminescence in Sm^{3+}/Er^{3+} doped host-sensitized $LaNbO_4$ phosphor by energy transfer, Ceram. Int. 46 (2020) 28373-28381.

[14] D.-M. Kepaptsoglou, K. Hadidi, O.-M. Løvvik, A. Magraso, T. Norby, A.E. Gunnæs, A. Olsen, Q.M. Ramasse, Interfacial charge transfer and chemical bonding in a Ni-$LaNbO_4$ cermet for proton-conducting solid-oxide fuel cell anodes, Chem. Mater. 24 (2012) 4152-4159.

[15] A. Magrasó, M.-L. Fontaine, Investigation of compatible anode systems for $LaNbO_4$-based electrolyte in novel proton conducting solid oxide fuel cells, J. Power Sources, 196 (2011) 10183-10190.

[16] H.M. Liu, H.Y. Yu, J.X. Wang, F. Xia, C. Wang, J.Z. Xiao, $LaNbO_4$ as an electrode material for mixed-potential CO gas sensors, Sensor Actuat. B-Chem. 352 (2022) 130981.

[17] S.L. Gai, C.X. Li, P.P. Yang, J. Lin, Recent progress in rare earth micro/nanocrystals: Soft chemical synthesis, luminescent properties, and biomedical applications, Chem. Rev. 114 (2014) 2343-2389.

[18] C.X. Li, J. Yang, Z.W. Quan, P.P. Yang, D.Y. Kong, J. Lin, Different microstructures of β-$NaYF_4$ fabricated by hydrothermal process: Effects of pH values and fluoride sources, Chem. Mater. 19 (2007) 4933-4942.

[19] Z.H. Wang, J.-G. Li, Q. Zhu, B.-N. Kim, X.D. Sun, Dicarboxylate mediated efficient morphology/phase tailoring of YPO_4:Ln^{3+} crystals and investigation of down-/up-conversion luminescence, CrystEngComm 19 (2017) 5230-5243.

[20] Bruker AXS TOPAS V4: General profile and structure analysis software for powder diffraction data-user's manual, Bruker AXS, Kalsruhe, Germany, 2008.

[21] C.F. Base, R.E. Mesmer, The hydrolysis of cations. John Wiley & Sons, New York,

1976.

[22] M. Aureliano, C.A. Ohlin, M.O. Vieira, M.P.M. Marques, W.H. Casey, L.A.E.B. de Carvalho, Characterization of decavanadate and decaniobate solutions by Raman spectroscopy, Dalton Trans. 45 (2016) 7391-7399.

[23] E.M. Villa, C.A. Ohlin, E. Balogh, T.M. Anderson, M.D. Nyman, W.H. Casey, Reaction dynamics of the decaniobate ion $[H_xNb_{10}O_{28}]^{(6-x)-}$ in water, Angew. Chem. Int. Ed, 47 (2008) 4844-4846.

[24] R.L. Rich, Inorganic reactions in water, Springer-Verlag, Berlin Heidelberg, 2007.

[25] I. Arellano, M. Nazarov, C.C. Byeon, E.-J. Popovici, H. Kim, H.C. Kang, D.Y. Noh, Luminescence and structural properties of $Y(Ta,Nb)O_4:Eu^{3+},Tb^{3+}$ phosphors, Mater. Chem. Phys. 119 (2010) 48-51.

[26] H.Q. Shi, Y. Liu, H.M. Xiao, S.Y. Fu, Tartrate-induced self-assembly of highly positively charged three-dimensional spiral $Cd(OH)_2$ flowers with largely exposed (001) plane, Cryst. Growth Des. 13 (2013) 1091-1098.

[27] Z.H. Wang, J.-G. Li, Q. Zhu, Z.R. Ai, X.D. Li, X.D. Sun, B.-N. Kim, Y. Sakka, EDTA-assisted phase conversion synthesis of $(Gd_{0.95}RE_{0.05})PO_4$ nanowires (RE = Eu, Tb) and investigation of photoluminescence, Sci. Technol. Adv. Mater. 18 (2017) 447-457.

[28] F. Wang, J. Wang, X.G. Liu, Direct evidence of a surface quenching effect on size-dependent luminescence of upconversion nanoparticles, Angew. Chem. Int. Ed. 49 (2010) 7456-7460.

[29] S.H. Huang, D. Wang, C.X. Li, L.Z. Wang, X. Zhang, Y. Wan, P.P. Yang,

Controllable synthesis, morphology evolution and luminescence properties of $NaLa(WO_4)_2$ microcrystals, 14 (2012) 2235-2244.

[30] S.K. Lee, H. Chang, C.-H. Han, H.-J. Kim, H.G. Jang, H.D. Park, Electronic structures and luminescence properties of $YNbO_4$ and $YNbO_4$:Bi, J. Solid State Chem. 156 (2001) 267-273.

[31] H.N. Huang, T. Wang, H.F. Zhou, D.P. Huang, Y.Q. Wu, G.J. Zhou, J.F. Hu, J. Zhan, Luminescence, energy transfer, and up-conversion mechanisms of Yb^{3+} and Tb^{3+} co-doped $LaNbO_4$, J. Alloys Compd. 702 (2017) 209-215.

[32] M. Huse, A.W.B. Skilbred, M. Karlsson, S.G. Eriksson, T. Norby, R. Haugsrud, C.S. Knee, Neutron diffraction study of the monoclinic to tetragonal structural transition in $LaNbO_4$ and its relation to proton mobility, J. Solid State Chem. 187 (2012) 27-34.

[33] L. Jian, C.M. Wayman, Monoclinic-to-tetragonal phase transformation in a ceramic rare-earth orthoniobate, $LaNbO_4$, J. Am. Ceram. Soc. 80 (1997) 803-806.

[34] R.D. Shannon, Revised effective ionic radii and systematic studies of interatomic distances in halides and chalcogenides, Acta. Cryst. A32(1976) 751-767.

[35] W.I.F. David, The high-temperature paraelastic structure of $LaNbO_4$, Mat. Res. Bull. 18 (1983) 749-756.

[36] B.R. Judd, Optical absorption intensities of rare-earth ions, Phys. Rev. 127 (1962) 750-761.

[37] Y.H. Kim, P. Arunkumar, B.Y. Kim, S. Unithrattil, E. Kim, S.-H. Moon, J.Y. Hyun, K.H. Kim, D. Lee, J.-S. Lee, W.B. Im, A zero-thermal-quenching phosphor, Nat.

Mater. 16 (2017) 543-550.

[38] P.P. Du, Q.H. Meng, X.J. Wang, Q. Zhu, X.D. Li, X.D. Sun, J.-G. Li, Sol-gel processing of Eu^{3+} doped $Li_6CaLa_2Nb_2O_{12}$ garnet for efficient and thermally stable red luminescence under near-ultraviolet/blue light excitation, Chem. Eng. J. 375 (2019) 121937.

[39] Y. Zhang, X.J. Li, K. Li, H.Z. Lian, M.M. Shang, J. Lin, Crystal-site engineering control for the reduction of Eu^{3+} to Eu^{2+} in $CaYAlO_4$: Structure refinement and tunable emission properties, ACS Appl. Mater. Interfaces 7 (2015) 2715-2725.

[40] W.G. Liu, X.J. Wang, Q. Zhu, J.-G. Li, Tb^{3+}/Mn^{2+} singly/doubly doped $Sr_3Ce(PO_4)_3$ for multi-color luminescence, excellent thermal stability and high-performance optical thermometry, J. Alloys Compd. 829 (2020) 154563.

[41] M. Zhao, Z.G. Xia, X.X. Huang, L.X. Ning, R. Gautier, M.S. Molokeev, Y.Y. Zhou, Y.-C. Chuang, Q.Y. Zhang, Q.L. Liu, K.R. Poeppelmeier, Li substituent tuning of LED phosphors with enhanced efficiency, tunable photoluminescence, and improved thermal stability, Sci. Adv. 5 (2019) eaav0363.

[42] Y. Gao, F. Huang, H. Lin, J.C. Zhou, J. Xu, Y.S. Wang, A novel optical thermometry strategy based on diverse thermal response from two intervalence charge transfer states, Adv. Funct. Mater. 26 (2016) 3139-3145.

[43] H.K. Liu, L.F. Mei, L.B. Liao, Y.Y. Zhang, Q.F. Guo, T.S. Zhou, Y.J. Wang, L. Li, Strategy for realizing ratiometric optical thermometry via efficient Tb^{3+}-Mn^{2+} energy transfer in novel apatite-type phosphor $Ca_9Tb(PO_4)_5(SiO_4)F_2$, J. Alloys Compd. 770 (2019) 1237-1243.

[44] M.Y. Ding, H.L. Zhang, D.Q. Chen, Q.W. Hu, J.H. Xi, Z.G. Ji, Color-tunable luminescence, energy transfer and temperature sensing behavior of hexagonal $NaYF_4:Ce^{3+}/Tb^{3+}/Eu^{3+}$ microcrystals, J. Alloys Compd. 672 (2016) 117-124.

[45] A.K. Singh, S.K. Singh, B.K. Gupta, R. Prakash, S.B. Rai, Probing a highly efficient dual mode: Down-upconversion luminescence and temperature sensing performance of rare-earth oxide phosphors, Dalton Trans. 42 (2013) 1065-1072.

[46] X.J. Wang, X.W. Feng, M.S. Molokeev, H.L. Zheng, Q.S. Wang, C.Y. Xu, J.-G. Li, Modulation of Bi^{3+} luminescence from broadband green to broadband deep red in Lu_2WO_6 by Gd^{3+} doping and its applications in high color rendering index white LED and near-infrared LED, Dalton Trans. 52 (2023) 2619-2630.